

Visualizing the breakdown of the quantum anomalous Hall effect

G. M. Ferguson¹, Run Xiao², Anthony R. Richardella², Austin Kaczmarek¹
Nitin Samarth², Katja C. Nowack^{1,3*}

¹Laboratory of Atomic and Solid-State Physics, Cornell University, Ithaca, NY 14853, USA

²Department of Physics, The Pennsylvania State University, University Park, 16802, Pennsylvania, USA

³Kavli Institute at Cornell for Nanoscale Science, Cornell University, Ithaca, NY 14853, USA

*To whom correspondence should be addressed; email: kcn34@cornell.edu

Abstract

The creation of topologically non-trivial matter across electronic, mechanical, cold-atom, and photonic platforms is advancing rapidly, yet understanding the breakdown of topological protection remains a major challenge. In this work, we use magnetic imaging combined with global electrical transport measurements to visualize the current-induced breakdown of the quantum anomalous Hall effect (QAHE) in a magnetically doped topological insulator. We find that dissipation emerges at localized hot spots near electrical contacts, where an abrupt change in Hall angle leads to significant distortions of the current density. Using the local magnetization as a proxy for electron temperature, we directly observe that the electrons are driven out of equilibrium with the lattice at the hot spots and throughout the device in the breakdown regime. By characterizing energy relaxation processes in our device, we show that the breakdown of quantization is governed entirely by electron heating, and that a vanishing thermal relaxation strength at millikelvin temperatures limits the robustness of the QAHE. Our findings provide a framework for diagnosing energy relaxation in topological materials and will guide realizing robust topological protection in magnetic topological insulators.

The quantum anomalous Hall effect (QAHE), characterized by a quantized Hall effect and a vanishing longitudinal resistance at zero magnetic field, is an example of a topologically protected state of matter [1]. Although the QAHE has potential applications in metrology [2, 3] as well as classical [4–7] and quantum information processing [8], experimental realizations of the QAHE remain limited to cryogenic temperatures and low bias currents. Understanding the microscopic origin of these limitations to the QAHE is therefore crucial for realizing a robust QAHE at higher temperatures and bias currents.

At sufficiently high temperatures or bias currents, all QAH systems undergo a breakdown process marked by the deviation of the electronic transport coefficients from their quantized values. Electrical transport measurements of breakdown have focused on magnetically doped topological insulators (TIs) in which the QAHE has been first realized [9]. The results have been interpreted using a range of models, including field-assisted variable range hopping [10], bootstrap electron heating [11] and electric field driven breakdown [12]. Although QAH systems are predicted to host topologically protected edge states, the role that these edge states play in the transport and breakdown of the QAHE remains controversial [12–17]. Despite this interest in understanding the breakdown of the QAHE, its microscopic nature remains unclear.

In this work, we use magnetic imaging combined with global electrical transport measurements to characterize the current-induced breakdown of the quantum anomalous Hall regime in the magnetically doped TI $\text{Cr}_{0.15}(\text{Bi}, \text{Sb})_{1.85}\text{Te}_3$. We find that the magnetization serves as a sensor of the local electron temperature, providing micrometer-scale information about where power is dissipated in our device. Simultaneously, we acquire images of the stray magnetic field produced by the current in the device, allowing us to determine the current distribution. For magnetic imaging, we use a scanning superconducting quantum interference device (SQUID) microscope [18], illustrated schematically in Fig. 1a. We approach a SQUID with a micrometer-scale pickup loop to the surface of a $\text{Cr}_{0.15}(\text{Bi}, \text{Sb})_{1.85}\text{Te}_3$ Hall bar. The device is fabricated on a SrTiO_3 substrate, which serves as a global back gate, and includes a top gate that was grounded for the measurements described here. Characterization of the electronic transport behavior and the current distribution in the channel in the low-bias limit was presented in Ref. [16] as Device C. To compare our sample with previous work on the breakdown of the QAHE, we present the temperature-dependent conductivity of our device in Supplementary Information Section 1.

In our measurements, several sources of stray magnetic fields are present. The static magnetization of the Cr-dopants produces a static field, which we detect as a DC signal, Φ_{DC} . We apply a bias current I_b at a frequency $f = 140.6$ Hz through the channel of the sample. The resulting alternating current generates a stray magnetic field at the same frequency. We detect the corresponding flux, Φ_{1f} , coupled into the SQUID pickup loop using lock-in amplification. In addition, we observe a second harmonic response, Φ_{2f} , at twice the excitation frequency, which we show below arises from small changes in the sample magnetization due to current-induced heating. In Fig. 1b, we present a Φ_{DC} image acquired after magnetizing the sample into the plane ($-z$). The Φ_{DC} image reveals the outline of the channel and two of the voltage probes. Figs. 1c and 1g show the simultaneously acquired Φ_{1f} and Φ_{2f} signals. The origins of Φ_{DC} , Φ_{1f} and Φ_{2f} signals are illustrated schematically in Fig. 1h. Further details on the sample fabrication, scanning SQUID measurements and lock-in detection scheme are provided in the Methods section.

The Φ_{1f} image corresponds to the stray magnetic field generated by the current distribution in the sample. A striking feature in the Φ_{1f} image (Fig. 1c) is the strong signal observed at the top corner of the interface between the gold contact and the $\text{Cr}_{0.15}(\text{Bi}, \text{Sb})_{1.85}\text{Te}_3$ channel which gradually evolves into a smooth gradient along the y direction further away from the contact.

To understand the current distribution in the vicinity of the contact, we performed electrostatic potential simulations of the interface between the metallic contact and $\text{Cr}_{0.15}(\text{Bi}, \text{Sb})_{1.85}\text{Te}_3$ channel. In this model, the $\text{Cr}_{0.15}(\text{Bi}, \text{Sb})_{1.85}\text{Te}_3$ film is represented by a resistor network [19], which includes elements to represent both the longitudinal and transverse resistivity with the resistor value determined by ρ_{xx} and ρ_{xy} measured under the same I_b and V_{BG} as the data in Fig. 1c. The metallic contacts are modeled by resistive elements that have a vanishing Hall effect. The result of the simulation is only sensitive to the change in Hall angle, θ_H , defined through $\tan \theta_H = \rho_{xy}/\rho_{xx}$ across the interface (see Supplementary Information: Resistor Network Model for details). In Fig 1d, we show the simulated electrostatic potential and current density for current applied to the contact. The dramatic change in θ_H at the interface between the contact and the channel strongly distorts the electrostatic potential and current distributions, leading to a concentration of the current density at one corner of the contact. To compare modeling and data, we calculate the magnetic field corresponding to the model current distribution, and convolve it with the imaging kernel of our SQUID. The resulting

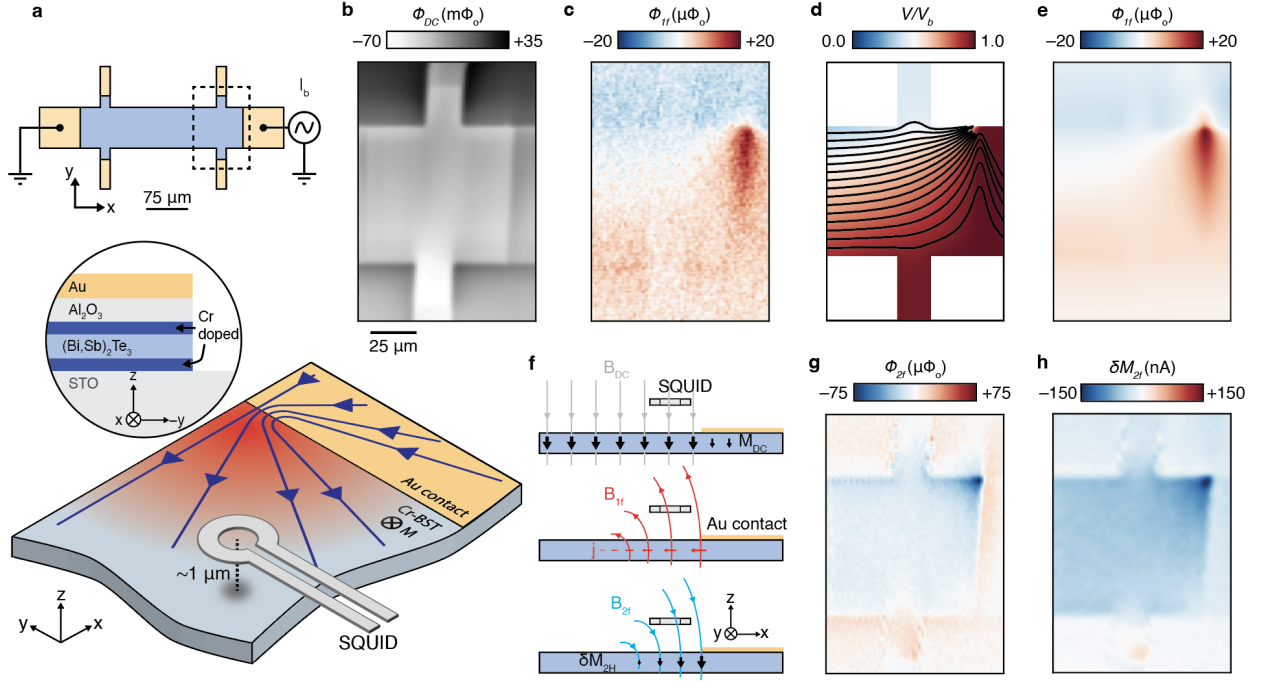


Figure 1: **Imaging currents and heating in a quantum anomalous Hall insulator.** **a**, Schematic of the measurement showing (top) the sample geometry and biasing scheme with the dashed box indicating the field of view, (middle) a cross-section of the magnetically doped topological insulator heterostructure, and (bottom) an illustration of the hot-spot region where current enters at the contact corner causing high local power dissipation. A SQUID with a micrometer-scale pickup loop detects magnetic signals from the sample. **b**, Image of the DC flux, Φ_{DC} , measured in the field of view indicated in **(a)**, top) with the sample magnetized into the plane. **c**, First harmonic SQUID signal, Φ_{1f} , co-recorded with **(b)**. The source-drain bias current I_b is 120 nA. **d**, Electrostatic potential distribution calculated using the measured longitudinal and Hall resistivities. Black lines show current streamlines calculated from the potential and the resistivity tensor. **e**, Model magnetic flux image obtained by convolving the the model current distribution in **(d)** with the SQUID's imaging kernel. **f**, Schematic illustrating the three modes of magnetic imaging demonstrated in **(b)**, **(c)** and **(g)**. The stray field from the sample magnetization couples a DC flux Φ_{DC} into the SQUID pickup loop (top). The transport current distribution couples a flux Φ_{1f} into the SQUID at the at the frequency of the excitation (middle). Changes in the sample magnetization due to heating in the sample couples a flux Φ_{2f} into the SQUID at twice the frequency of the excitation (bottom). **g**, Second harmonic SQUID signal, Φ_{2f} co-recorded with **(c)**. **h**, Change in the sample magnetization δM_{2f} induced by bias-induced heating, reconstructed from **(g)**. Data shown here is collected at base temperature of our dilution refrigerator, ~ 15 mK.

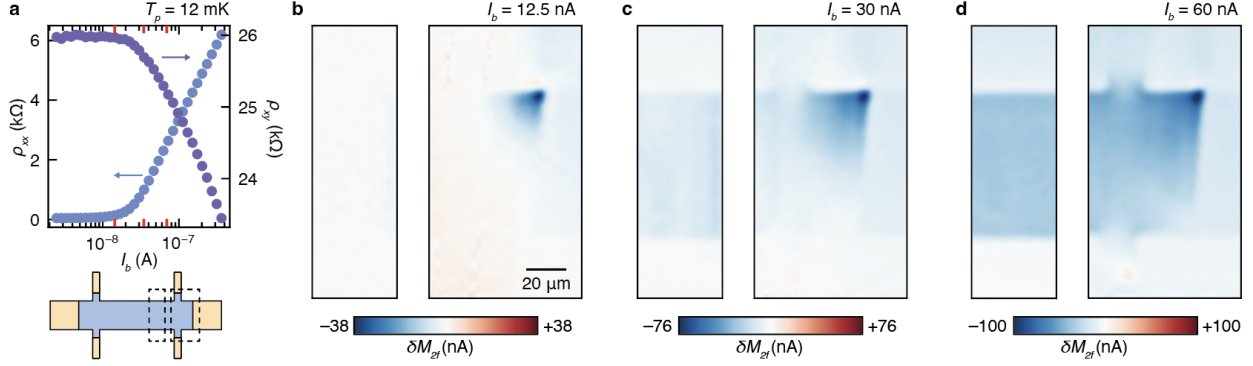


Figure 2: **QAH breakdown via bias-induced heating** **a**, Longitudinal (ρ_{xx}) and Hall (ρ_{xy}) resistivities versus bias current (I_b). Red tick marks indicate bias points for images in **b-d**, and their locations are depicted schematically at the bottom of the panel. **b**, δM_{2f} images for $I_b = 12.5$ nA below the breakdown of the QAHE. Strong signatures of heating are observed near the hot-spot, but not near the voltage probes or in the channel. **c**, δM_{2f} images for $I_b = 30$ nA at the onset of breakdown showing signatures of heating near the voltage probes and in the channel. **d**, δM_{2f} images at $I_b = 60$ nA above the breakdown current for the QAHE with nearly uniform heating signatures away from the hot-spot.

model Φ_{1f} image, shown in Fig 1e, quantitatively captures the measured Φ_{1f} image. In Supplemental Fig. 2, we show that we have similar quantitative agreement between our magnetic imaging and modeling as we tune θ_H with the back gate voltage. In a separate manuscript, we examine additional contributions to Φ_{1f} arising from an interplay of bias-induced shifts in the chemical potential and corresponding changes in the magnetization at values of I_b substantially exceeding those considered here [20].

In Fig. 1g, we find that Φ_{2f} has a pronounced signal in the corner of the contact coinciding with the “hot-spot” observed in the current density. The sign, spatial structure and amplitude of the Φ_{2f} signal are consistent with a small demagnetization of the sample, which we establish below is in response to current-induced heating of the electrons. Fig. 1h shows the corresponding change in sample magnetization, δM_{2f} reconstructed from Φ_{2f} . The change in magnetization is strongest at the “hot-spot” where Figs. 1c-e indicate the current density is the highest, and we expect the most significant heating. In agreement with the current density, the hot-spot moves from the top to the bottom of the contact when the magnetization is reversed (Extended Data Fig. 1).

Our observations bear a striking resemblance to work on dissipation in the integer quantum Hall regime in GaAs/AlGaAs heterostructures. Early work utilizing the fountain effect in a superfluid helium film to monitor the dissipation in a Hall bar device showed that power dissipation was highest in the two opposite corners of current-injecting contacts, with the corner determined by the sign of the magnetic field [21, 22]. Similarly, spatially resolved cyclotron emission studies revealed enhanced emission near the current entry and exit corners [23, 24].

Next, we focus on images of δM_{2f} as we vary the applied current. Fig. 2a shows ρ_{xx} and ρ_{xy} as a function of I_b . At low values of I_b , the sample exhibits the QAHE: the Hall resistivity is quantized in units of h/e^2 and the longitudinal resistivity ρ_{xx} is vanishing ($\rho_{xx} \approx 45 \Omega$). As I_b is increased beyond ~ 20 nA, ρ_{xx} increases and quantization of ρ_{xy} is lost, indicating the breakdown of the QAHE.

In Figs. 2b-d we show the reconstructed δM_{2f} at three representative values of I_b . At $I_b = 12.5$ nA (Fig. 2b), which is below the breakdown threshold, no heating is observed in the channel (left), however signatures of heating are still evident at the contact hot-spot (right). For $I_b = 30$ nA, the breakdown of the QAHE begins. ρ_{xx} is finite, and a heating signal appears both in the channel (right) as well as near the contact region (left). By the time I_b reaches 60 nA (Fig. 2d), we observe a more pronounced heating signal throughout the channel. A strong correlation between the magnitude of δM_{2f} and the electrical transport data is clear. A strong δM_{2f} consistently appears near the corner of the contact, where the current density is so high that breakdown is induced locally, even when dissipation measured by ρ_{xx} in the channel is low. Once I_b becomes large enough to cause an increase in ρ_{xx} as measured in transport, a corresponding δM_{2f} is observed throughout the entire device channel.

To study the correspondence between electrical transport data and the observed δM_{2f} in more detail, we introduce a thermal model of the system, schematically illustrated in Fig. 3a. This model consists of two subsystems: the electrons, described by a temperature T_e , and the lattice at a temperature T_p . Within our model, the electronic subsystem absorbs energy at a rate given by $P_{in} = R_{xx} I_b^2$ with R_{xx} a function of T_e . The electrons dissipate energy absorbed from the externally applied bias to the lattice at temperature T_p through an effective thermal resistance R_{th} , which represents all thermal relaxation processes between the electrons and their environment.

To characterize R_{th} , we apply the 3ω technique, which allows us to use the temperature dependence of R_{xx} to detect changes in T_e induced by I_b [25, 26]. When R_{xx} depends on T_e , changes to T_e induced by I_b generate a third-harmonic voltage drop over the sample V_{3f} , due to variations in the sample temperature and resistance during the duty-cycle of the lock-in excitation. The amplitude of V_{3f} depends on the temperature dependence of R_{xx} and R_{th} alone, allowing us to characterize R_{th} via measurements of ρ_{xx} and the bias and temperature dependence of V_{3f} . Further details of the 3ω technique as well as consistency checks are presented in the Methods and Supplementary information.

In Fig. 3b, we show the I_b and T_p dependence of the longitudinal resistance R_{xx} for our device. At each T_p , R_{xx} is minimized and independent of bias for low values of I_b , indicating that $T_p = T_e$ at low bias. From this low-bias data, we determine the dependence of R_{xx} on T_e . We then use this dependence to extract R_{th} from the measured V_{3f} , as shown in Fig. 3c. We find that R_{th} follows a power-law temperature dependence given by $R_{th} = (A\Sigma)^{-1} T^{-n}$ where A is the area of the $\text{Cr}_{0.15}(\text{Bi}, \text{Sb})_{1.85}\text{Te}_3$ channel and Σ characterizes the strength of the energy relaxation processes in our $\text{Cr}_{0.15}(\text{Bi}, \text{Sb})_{1.85}\text{Te}_3$ device. A fit to the temperature dependence of R_{th} yields best-fit parameters $n = 4.0 \pm 0.1$ and $\Sigma = 10(2) \text{ Wm}^{-2}\text{K}^{-5}$.

Our phenomenological model for energy relaxation in our device does not assume a specific microscopic process described by R_{th} . Previous work on energy relaxation at millikelvin temperatures in metals [27, 28], bulk semiconductors [29], and GaAs heterostructures in the integer quantum Hall regime [30, 31] have consistently identified power-law energy relaxation processes, $R_{th} \sim T^{-\alpha}$, with α between 3 and 5, depending on the material system. In these studies, R_{th} is attributed to electron-phonon coupling. In $\text{Cr}_{0.15}(\text{Bi}, \text{Sb})_{1.85}\text{Te}_3$, direct electron-phonon mediated energy relaxation is also a plausible microscopic process which establishes a thermal link between the electrons and the environment. Additionally, given the magnetic order in $\text{Cr}_{0.15}(\text{Bi}, \text{Sb})_{1.85}\text{Te}_3$, energy relaxation may also have contributions from collective excitations associated with the magnetization. The R_{th} that we report represents the combined effect of all energy relaxation processes.

With the temperature dependence of R_{th} established, we can estimate T_e for each combination of T_p and I_b . For electrons and phonons initially in equilibrium at temperature T , $dP_{out} = R_{th}(T)^{-1} dT$ represents the incremental increase in the power dissipated to the environment for an incremental increase in the electron temperature dT . In steady state, the input power to the electronic subsystem P_{in} is equal to the power dissipated to the environment. Integrating dP_{out} from T_p to T_e to obtain P_{out} , and setting $P_{in} = P_{out}$ yields,

$$T_e = \left[\frac{5P_{in}}{A\Sigma} + T_p^5 \right]^{1/5}, \quad (1)$$

where we have used $R_{th} = (A\Sigma)^{-1} T^{-4}$, based on our 3ω measurements. Since P_{in} depends on T_e through the temperature dependence of R_{xx} , we solve Eq. 1 numerically for T_e using our measurements of R_{th} and R_{xx} . In Fig. 3d, we re-plot the data from Fig. 3b as a function of the resulting T_e calculated with our heating model. The data collapse onto a single curve, independent of the specific values of T_p and I_b at which R_{xx} was measured. Additionally, we highlight in Fig. 3d the values of R_{xx} measured at the lowest bias limit where $T_e = T_p$. The re-scaled data for each combination of T_p and I_b agree closely with this low-bias curve. The same analysis also allows us to collapse the R_{xy} data onto a single curve independent of T_p and I_b (Supplemental Information: Consistency checks for the 3ω method.).

The collapse of the electronic transport coefficients onto a single curve indicates that nearly all changes in the sample's resistivity with both I_b and T_p can be attributed to changes in the electron temperature T_e . Consequently, the breakdown of the QAHE in our device is solely governed by T_e . While changing T_p , I_b , or both may induce breakdown, these changes ultimately generate a corresponding change in T_e , restoring balance between P_{in} and P_{out} .

With the energy absorption and relaxation processes characterized, we now turn to examining the local

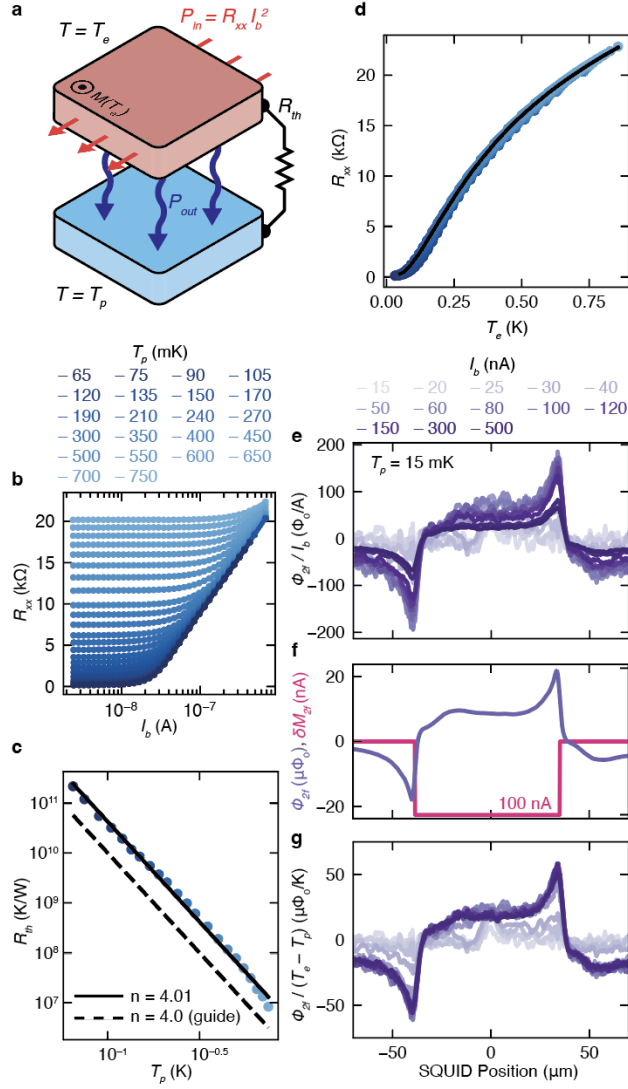


Figure 3: **Hot electrons and energy relaxation** **a**, Illustration of the thermal relaxation model. Electrons absorb power P_{in} from the bias current. Power is dissipated to the environment through the thermal resistance R_{th} . **b**, Longitudinal resistance R_{xx} as a function of bias current I_b and lattice temperature T_p . **c**, Temperature dependence of the thermal relaxation strength R_{th} , measured via the 3ω method at the same T_p as in **(b)**. **d**, R_{xx} from **(b)** plotted versus the electron temperature T_e inferred from the model in **(a)** and characterized in **b**, **c**. The data collapse onto a single curve, indicating that R_{xx} depends solely T_e . The black curve shows the temperature dependence of R_{xx} for low bias ($I_b = 2.45$ nA) for comparison. **e**, Φ_{2f} acquired along a line over the device channel at $T_p = 15$ mK for various I_b . **f**, Model of a spatially uniform demagnetization of the channel δM_{2f} of 100 nA is shown in blue. Convolution of the δM_{2f} signal with the SQUID's imaging kernel yields the corresponding modeled flux Φ_{2f} . **g**, Data from **(e)**, normalized by the electron heating amplitude $T_e - T_p$ calculated from the hot electron model. Traces with $T_e - T_p < 25$ mK are omitted for clarity.

magnetic signatures of heating. In Fig. 3e, we plot Φ_{2f} normalized by I_b acquired along a line between the voltage probes in our Hall bar at various values of I_b . At the lowest values of I_b , there is minimal spatial structure in Φ_{2f} , as dissipation in the channel is low and changes in T_e in response to I_b are small. Fig. 3f shows a simulated magnetic flux profile for a uniform sample demagnetization across the channel width. At higher bias currents, the spatial profile of Φ_{2f} in Fig. 3e closely resembles this model for a uniform demagnetization. Fig. 3e reveals that the magnitude of Φ_{2f}/I_b obeys a sub-linear dependence on I_b : traces at the highest values of I_b exhibit a smaller peak-to-peak amplitude than those at intermediate values of I_b . An interpretation of Φ_{2f} in terms of a response proportional to the dissipated power, $\Phi_{2f} \sim P_{in} \sim R_{xx}I_b^2$, is incompatible with the data.

To understand the scaling of Φ_{2f} , we re-plot the traces from Fig. 3e in Fig. 3g, now normalizing Φ_{2f} by the temperature difference between the electrons and phonons, $T_e - T_p$, as predicted by our heating model. This separates the curves into two classes: curves for I_b below ~ 30 nA exhibit little spatial structure, whereas above this level they collapse onto a single profile. Notably, $I_b \sim 30$ nA is also the value beyond which R_{xx} in Fig. 3 rises significantly. Taken together, these observations indicate that Φ_{2f} is proportional to changes in T_e . By tracking changes in T_e through corresponding changes in the magnetization, we spatially resolve regions of the sample where T_e is driven out of equilibrium by the bias current with micron-scale spatial resolution. We repeated this measurement and analysis at several values of T_p , and present the results in Extended Data Fig. 2. As T_p increases, the thermal coupling between the electrons and lattice becomes stronger and the bias current required to drive T_e above T_p increases. Similarly, increasing T_p also changes the heating signatures in the vicinity of the hot spot. In Extended Data Fig. 3, we show images of Φ_{DC} , Φ_{1f} , Φ_{2f} , and reconstructed δM_{2f} acquired near the contact interface, with $T_p = 750$ mK and same bias current, $I_b = 150$ nA, as the data in Fig. 1. Although signatures of heating are dramatically weakened by raising T_p , we still observe heating effects localized at the hot spot.

The temperature differences generated between the electrons and the lattice during breakdown are substantial. Our measurements indicate that even for modest bias currents of ~ 100 nA, a temperature difference of several hundred mK is generated between the electronic and lattice subsystems. The amplitude of the temperature differences generated between T_e and T_p for the range of bias currents and T_p explored in this work is presented in Extended Data Figure 4. The heating effect is even more pronounced near the contacts, where the current density at the hot spot is high regardless of the total source drain bias. In this region, substantial heating occurs even when ρ_{xx} near the voltage probes approaches zero. The large electron and phonon temperature differences may play a role in a number of phenomena reported in transport experiments, including electronic switching of magnetically doped topological insulators driven by source-drain bias currents several orders of magnitude larger than those used here [7, 32].

To understand the details of energy dissipation near the hot spot, we extend our resistor network model to account for heating effects. Using the electrostatic potential distribution obtained for $T_e = T_p$, we calculate the local power dissipation per unit area, p_{in} within the device. By identifying P_{in}/A with p_{in} in Eq. 1, we can use Σ extracted from the 3ω method to determine the local T_e distribution. Using this temperature distribution, we update the local conductivity values and re-calculate the electrostatic potential distribution, p_{in} and T_e . After a few iterations, these calculations converge to a self-consistent temperature distribution for a given combination of I_b and T_p , from which all other properties of the device may be calculated. In this model, we neglect the effects of thermal transport within the electronic subsystem and consider only the energy transport processes described by R_{th} which relax energy out of the electronic subsystem to the environment. We discuss the effects of thermal transport through the electrons to the metallic contacts below. Further details of the self-consistent calculations are presented in Supplementary Information: Resistor network model.

In Fig. 4a, we show the electron heating ($T_e - T_p$) for the experimental conditions ($T_p < 50$ mK, $I_b = 12.5$ nA) and field of view as in Fig. 2b. Substantial heating is found in the vicinity of the hot-spot, where the current density is highest. Due to the high conductivity of the metallic contact, p_{in} is several orders of magnitude smaller than in the semiconducting channel, and heating in the contacts is negligible in our model. Away from the contact area, we do not find substantial heating for $I_b = 12.5$ nA. In Fig. 4b, we show results for $I_b = 60$ nA, a bias current above the threshold for breakdown of the QAHE in our device (see Fig. 2). In contrast to $I_b = 12.5$ nA, a uniform temperature difference $T_e - T_p \approx 75$ mK develops in the device channel.

A quantitative comparison of this calculation to images of Φ_{2f} requires the temperature dependence of the

sample magnetization $M(T)$. Given that typical values of T_e are small compared to the Curie temperature of ~ 20 K under all conditions investigated in this work [1], we adopt the approximation $M(T) \approx M_o - \alpha T$, appropriate for superparamagnetic thin-films far below the Curie temperature [33–35]. For the Φ_{2f} acquired over the channel in Fig. 3e, we find that $\alpha = 300$ nA/K provides good agreement between the measured Φ_{2f} data and T_e predicted by the model. Compared to the static magnetization of the sample, M_o , heating-induced changes in the magnetization are small. From Φ_{DC} measured scanning the SQUID over the channel, we estimate that $M_o \approx 100$ μ A $\gg \alpha 1$ K ≈ 300 nA, where a temperature change of ~ 1 K represents a rough upper bound for the heating effects in our sample. This estimate of $M_o \approx 100$ μ A gives a magnetization per Cr-doped layer which is consistent with previous measurements in similar $\text{Cr}_{0.15}(\text{Bi}, \text{Sb})_{1.85}\text{Te}_3$ samples [34].

In Fig. 4c and d, we show simulated $\Phi_{2f,m}$ images obtained by calculating $\delta M_{2f,m}$ using α and the local T_e , calculating the corresponding stray magnetic field and convolving with the imaging kernel of our SQUID. For comparison, Fig. 4e and f show the corresponding Φ_{2f} images, acquired under experimental conditions matching the model, with additional comparisons for other values of I_b presented in Extended Data Figure 5. Despite its simplicity, the model shows good agreement with the data: strong Φ_{2f} signals consistently appear at the hot-spots indicating large temperature differences between the electrons and phonons. Away from the contacts, Φ_{2f} signals are associated with the onset of dissipation in the channel and the breakdown of the QAHE detected in electrical transport measurements.

In the simulation, we assume that the thermal conduction through the electronic system is negligible compared to R_{th} . Although this assumption yields good quantitative agreement with the Φ_{2f} data away from the contacts, the model systematically over-estimates the Φ_{2f} signal at the hot spot. Both our data and simulations indicate that the metallic contacts remain near T_p , leading to pronounced temperature gradients near the contacts. A plausible explanation for the discrepancy is the electronic thermal conduction providing cooling from the metallic contact at the semiconductor-metal interface. An estimate of the electronic contribution to the thermal conductance indicates that this cooling pathway is important only within a few micrometers of the semiconductor-metal interface (See Supplementary Section: Estimate of the Electronic Thermal Conductance). Due to the vanishing σ_{xx} at low temperatures, energy absorbed by the electrons in the channel cannot be transported to the contacts before it is relaxed directly through R_{th} .

Heating effects have previously been considered in the context of the breakdown of the integer quantum Hall effect (IQHE). In high mobility samples, the breakdown of the IQHE was found to be non-local [36, 37], with hot electrons diffusing over hundreds of micrometers. In contrast, in our measurements, as well as in transport measurements on similar $\text{Cr}_{0.15}(\text{Bi}, \text{Sb})_{1.85}\text{Te}_3$ samples [15], the breakdown phenomenology may be understood without introducing non-local behavior. This discrepancy may qualitatively be understood in terms heavy doping required to realize the QAHE in MTIs, which severely limits the carrier mobility. The QAHE has been realized in a variety of material platforms including $(\text{Bi}, \text{Sb})_{1.85}\text{Te}_3$ doped with different magnetic elements, stoichiometric magnetic topological insulators [38], and van der Waals heterostructures [39–43]. We anticipate that differences in the carrier mean-free-path across material systems will qualitatively alter the nature of energy absorption and relaxation in the QAH regime. In particular, measurements on higher mobility QAH systems may identify non-local heating and breakdown behavior similar to those detected in the IQHE in GaAs.

Although energy relaxation processes impose fundamental limitations on the performance of any device which utilizes the novel electronic behavior exhibited by quantum materials, direct experimental access to this information remains scarce [44, 45]. We have developed a method of experimentally monitoring power dissipation in $\text{Cr}_{0.15}(\text{Bi}, \text{Sb})_{1.85}\text{Te}_3$ samples using a scanning SQUID microscope. By combining this approach with transport measurements of the energy relaxation rate, we identified the central role that hot electrons play in regulating the breakdown of the QAHE. We find that breakdown is well described by a local picture of energy relaxation. As the breakdown of the QAHE is investigated in new materials systems, particularly those with higher mobility, our approach will guide the characterization of breakdown as the QAHE is pushed towards higher temperatures and current densities.

Acknowledgements

We acknowledge helpful discussions at the early stages of this work with Erik Henriksen, Brad Ramshaw, Gaël Grissonnache, and David Goldhaber-Gordon. Work at Cornell University was primarily supported by the U.S. Department of Energy, Office of Basic Energy Sciences, Division of Materials Sciences and

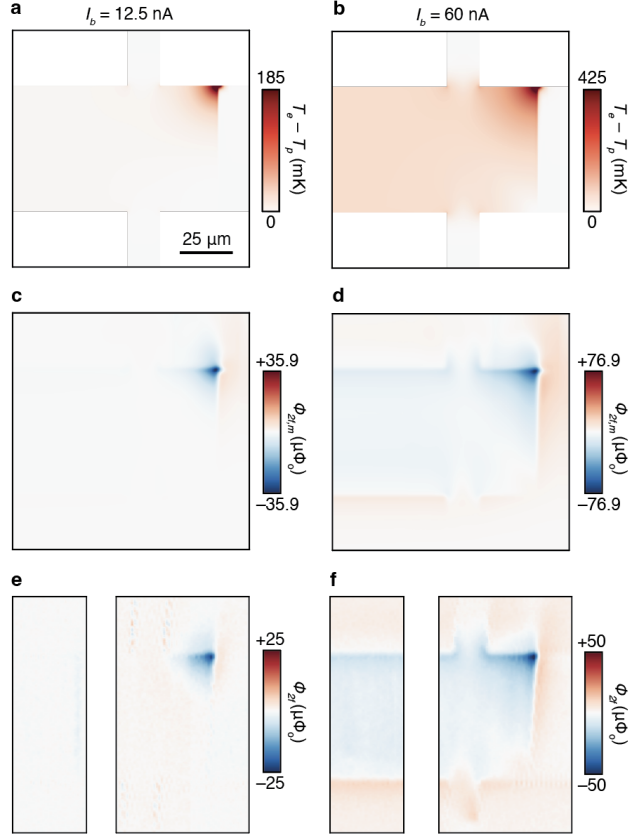


Figure 4: **Imaging hot electrons** **a**, Spatial profile of the heating effect, $T_e - T_p$, calculated self-consistently with the current and electrostatic potential distributions, using the thermal relaxation strength extracted from the 3ω technique. Model I_b and T_p are chosen to match the experimental conditions in Fig. 2b, with I_b below the breakdown current for the QAHE. **b**, Same as **(a)**, with I_b and T_p adjusted to the experimental conditions of Fig. 2d, with I_b above the breakdown current for the QAHE. **c**, Model $\Phi_{2f,m}$ calculated using the temperature profile in **(a)**, assuming a temperature dependence of the magnetization with $\alpha = 300$ nA/K. **d**, Same as **(c)**, but using the temperature profile in **(b)**. **e**, **f** Experimental Φ_{2f} used to reconstruct δM_{2f} shown in **(e)** Fig. 2b and **(f)** in Fig. 2d.

Engineering, under award DE-SC0015947 with additional support from a New Frontier Grant awarded by Cornell University's College of Arts & Sciences. Sample synthesis and fabrication at Penn State was supported by the Penn State 2DCC-MIP under NSF Grant Nos. DMR-1539916 and DMR-2039351.

References

- [1] Cui-Zu Chang, Chao-Xing Liu, and Allan H. MacDonald. Colloquium: Quantum anomalous hall effect. *Rev. Mod. Phys.*, 95:011002, 2023.
- [2] Yuma Okazaki, Takehiko Oe, Minoru Kawamura, Ryutaro Yoshimi, Shuji Nakamura, Shintaro Takada, Masataka Mogi, Kei S Takahashi, Atsushi Tsukazaki, Masashi Kawasaki, et al. Quantum anomalous Hall effect with a permanent magnet defines a quantum resistance standard. *Nature Physics*, 18(1): 25–29, 2022.
- [3] Linsey K Rodenbach, Alireza R Panna, Shamith U Payagala, Ilan T Rosen, Molly P Andersen, Peng Zhang, Lixuan Tai, Kang L Wang, Dean G Jarrett, Randolph E Elmquist, et al. Metrological assessment of quantum anomalous Hall properties. *Physical Review Applied*, 18(3):034008, 2022.
- [4] Yabin Fan, Pramey Upadhyaya, Xufeng Kou, Murong Lang, So Takei, Zhenxing Wang, Jianshi Tang, Liang He, Li-Te Chang, Mohammad Montazeri, et al. Magnetization switching through giant spin-orbit torque in a magnetically doped topological insulator heterostructure. *Nature Materials*, 13(7):699–704, 2014.
- [5] Yabin Fan, Xufeng Kou, Pramey Upadhyaya, Qiming Shao, Lei Pan, Murong Lang, Xiaoyu Che, Jianshi Tang, Mohammad Montazeri, Koichi Murata, et al. Electric-field control of spin-orbit torque in a magnetically doped topological insulator. *Nature Nanotechnology*, 11(4):352–359, 2016.
- [6] K Kondou, R Yoshimi, A Tsukazaki, Y Fukuma, J Matsuno, KS Takahashi, M Kawasaki, Y Tokura, and Y Otani. Fermi-level-dependent charge-to-spin current conversion by dirac surface states of topological insulators. *Nature Physics*, 12(11):1027–1031, 2016.
- [7] Wei Yuan, Ling-Jie Zhou, Kaijie Yang, Yi-Fan Zhao, Ruoxi Zhang, Zijie Yan, Deyi Zhuo, Ruobing Mei, Yang Wang, Hemian Yi, et al. Electrical switching of the edge current chirality in quantum anomalous Hall insulators. *Nature Materials*, 23(1):58–64, 2024.
- [8] Biao Lian, Xiao-Qi Sun, Abolhassan Vaezi, Xiao-Liang Qi, and Shou-Cheng Zhang. Topological quantum computation based on chiral Majorana fermions. *Proceedings of the National Academy of Sciences*, 115(43):10938–10942, 2018.
- [9] Cui-Zu Chang, Jinsong Zhang, Xiao Feng, Jie Shen, Zuocheng Zhang, Minghua Guo, Kang Li, Yunbo Ou, Pang Wei, Li-Li Wang, et al. Experimental observation of the quantum anomalous Hall effect in a magnetic topological insulator. *Science*, 340(6129):167–170, 2013.
- [10] Minoru Kawamura, Ryutaro Yoshimi, Atsushi Tsukazaki, Kei S Takahashi, Masashi Kawasaki, and Yoshinori Tokura. Current-driven instability of the quantum anomalous Hall effect in ferromagnetic topological insulators. *Physical Review Letters*, 119(1):016803, 2017.
- [11] Eli J Fox, Ilan T Rosen, Yanfei Yang, George R Jones, Randolph E Elmquist, Xufeng Kou, Lei Pan, Kang L Wang, and D Goldhaber-Gordon. Part-per-million quantization and current-induced breakdown of the quantum anomalous Hall effect. *Physical Review B*, 98(7):075145, 2018.
- [12] Gertjan Lippertz, Andrea Bliesener, Anjana Uday, Lino MC Pereira, AA Taskin, and Yoichi Ando. Current-induced breakdown of the quantum anomalous Hall effect. *Physical Review B*, 106(4):045419, 2022.
- [13] Cui-Zu Chang, Weiwei Zhao, Duk Y Kim, Peng Wei, Jainendra K Jain, Chaoxing Liu, Moses HW Chan, and Jagadeesh S Moodera. Zero-field dissipationless chiral edge transport and the nature of dissipation in the quantum anomalous Hall state. *Physical Review Letters*, 115(5):057206, 2015.

- [14] Linsey K Rodenbach, Ilan T Rosen, Eli J Fox, Peng Zhang, Lei Pan, Kang L Wang, Marc A Kastner, and David Goldhaber-Gordon. Bulk dissipation in the quantum anomalous Hall effect. *APL Materials*, 9:081116, 2021.
- [15] Ilan T Rosen, Molly P Andersen, Linsey K Rodenbach, Lixuan Tai, Peng Zhang, Kang L Wang, MA Kastner, and David Goldhaber-Gordon. Measured potential profile in a quantum anomalous Hall system suggests bulk-dominated current flow. *Physical Review Letters*, 129(24):246602, 2022.
- [16] GM Ferguson, Run Xiao, Anthony R Richardella, David Low, Nitin Samarth, and Katja C Nowack. Direct visualization of electronic transport in a quantum anomalous Hall insulator. *Nature Materials*, 22(9):1100–1105, 2023.
- [17] Benoit Doucot, Dmitry Kovrizhin, and Roderich Moessner. Meandering conduction channels and the tunable nature of quantized charge transport. *Proceedings of the National Academy of Sciences*, 121(39):e2410703121, 2024. doi: 10.1073/pnas.2410703121.
- [18] David Low, GM Ferguson, Alexander Jarjour, Brian T Schaefer, Maja D Bachmann, Philip JW Moll, and Katja C Nowack. Scanning SQUID microscopy in a cryogen-free dilution refrigerator. *Review of Scientific Instruments*, 92(8), 2021.
- [19] HH Sample, WJ Bruno, SB Sample, and EK Sichel. Reverse-field reciprocity for conducting specimens in magnetic fields. *Journal of Applied Physics*, 61(3):1079–1084, 1987.
- [20] GM Ferguson, Run Xiao, Anthony R Richardella, Austin Kaczmarek, Nitin Samarth, and Katja C Nowack. Imaging signatures of edge currents in a magnetic topological insulator. *arXiv preprint arXiv:2501.11666*, 2025.
- [21] U Klass, W Dietsche, K Von Klitzing, and K Ploog. Fountain-pressure imaging of the dissipation in quantum-Hall experiments. *Physica B: Condensed Matter*, 169(1-4):363–367, 1991.
- [22] U Klass, W Dietsche, K von Klitzing, and K Ploog. Image of the dissipation in gated quantum Hall effect samples. *Surface science*, 263(1-3):97–99, 1992.
- [23] Y Kawano, Y Hisanaga, and S Komiyama. Cyclotron emission from quantized Hall devices: Injection of nonequilibrium electrons from contacts. *Physical Review B*, 59(19):12537, 1999.
- [24] S Komiyama, H Sakuma, K Ikushima, and K Hirakawa. Electron temperature of hot spots in quantum Hall conductors. *Physical Review B*, 73(4):045333, 2006.
- [25] David G Cahill and Robert O Pohl. Thermal conductivity of amorphous solids above the plateau. *Physical review B*, 35(8):4067, 1987.
- [26] David G Cahill. Thermal conductivity measurement from 30 to 750 k: the 3ω method. *Review of Scientific Instruments*, 61(2):802–808, 1990.
- [27] Michael Lee Roukes, MR Freeman, RS Germain, RC Richardson, and MB Ketchen. Hot electrons and energy transport in metals at millikelvin temperatures. *Physical Review Letters*, 55(4):422, 1985.
- [28] FC Wellstood, C Urbina, and John Clarke. Hot-electron effects in metals. *Physical Review B*, 49(9):5942, 1994.
- [29] J Zhang, W Cui, M Juda, D McCammon, RL Kelley, SH Moseley, CK Stahle, and AE Szymkowiak. Non-ohmic effects in hopping conduction in doped silicon and germanium between 0.05 and 1 k. *Physical Review B*, 57(8):4472, 1998.
- [30] Edmond Chow and HP Wei. Experiments on inelastic scattering in the integer quantum Hall effect. *Physical Review B*, 52(19):13749, 1995.
- [31] Edmond Chow, HP Wei, SM Girvin, and M Shayegan. Phonon emission from a 2d electron gas: Evidence of transition to the hydrodynamic regime. *Physical Review Letters*, 77(6):1143, 1996.

- [32] Erik Zimmermann, Justus Teller, Michael Schleenvoigt, Gerrit Behner, Peter Schüffelgen, Hans Lüth, Detlev Grützmacher, and Thomas Schäpers. Current-induced magnetization switching in a magnetic topological insulator heterostructure. *Physical Review Materials*, 8(2):026201, 2024.
- [33] ZQ Qiu, SH Mayer, CJ Gutierrez, H Tang, and JC Walker. Thermal magnetic relaxation in quasi-two-dimensional Fe films. *Physical Review Letters*, 63(15):1649, 1989.
- [34] Ella O Lachman, Andrea F Young, Anthony Richardella, Jo Cuppens, HR Naren, Yonathan Anahory, Alexander Y Meltzer, Abhinav Kandala, Susan Kempinger, Yuri Myasoedov, et al. Visualization of superparamagnetic dynamics in magnetic topological insulators. *Science Advances*, 1(10):e1500740, 2015.
- [35] Ella O Lachman, Masataka Mogi, Jayanta Sarkar, Aviram Uri, Kousik Bagani, Yonathan Anahory, Yuri Myasoedov, Martin E Huber, Atsushi Tsukazaki, Masashi Kawasaki, et al. Observation of superparamagnetism in coexistence with quantum anomalous Hall $C=\pm 1$ and $C = 0$ Chern states. *npj Quantum Materials*, 2(1):70, 2017.
- [36] S Komiyama, Y Kawaguchi, T Osada, and Y Shiraki. Evidence of nonlocal breakdown of the integer quantum Hall effect. *Physical Review Letters*, 77(3):558, 1996.
- [37] II Kaya, G Nachtwei, K Von Klitzing, and K Eberl. Spatial evolution of hot-electron relaxation in quantum Hall conductors. *Physical Review B*, 58(12):R7536, 1998.
- [38] Yujun Deng, Yijun Yu, Meng Zhu Shi, Zhongxun Guo, Zihan Xu, Jing Wang, Xian Hui Chen, and Yuanbo Zhang. Quantum anomalous Hall effect in intrinsic magnetic topological insulator MnBi_2Te_4 . *Science*, 367(6480):895–900, 2020.
- [39] M Serlin, CL Tschirhart, H Polshyn, Y Zhang, J Zhu, K Watanabe, T Taniguchi, L Balents, and AF Young. Intrinsic quantized anomalous Hall effect in a moiré heterostructure. *Science*, 367(6480):900–903, 2020.
- [40] Tingxin Li, Shengwei Jiang, Bowen Shen, Yang Zhang, Lizhong Li, Zui Tao, Trithep Devakul, Kenji Watanabe, Takashi Taniguchi, Liang Fu, et al. Quantum anomalous Hall effect from intertwined moiré bands. *Nature*, 600(7890):641–646, 2021.
- [41] Tonghang Han, Zhengguang Lu, Giovanni Scuri, Jiho Sung, Jue Wang, Tianyi Han, Kenji Watanabe, Takashi Taniguchi, Hongkun Park, and Long Ju. Correlated insulator and Chern insulators in pentalayer rhombohedral-stacked graphene. *Nature Nanotechnology*, 19(2):181–187, 2024.
- [42] Tonghang Han, Zhengguang Lu, Yuxuan Yao, Jixiang Yang, Junseok Seo, Chiho Yoon, Kenji Watanabe, Takashi Taniguchi, Liang Fu, Fan Zhang, et al. Large quantum anomalous Hall effect in spin-orbit proximitized rhombohedral graphene. *Science*, 384(6696):647–651, 2024.
- [43] Wenjin Zhao, Kaifei Kang, Yichi Zhang, Patrick Knüppel, Zui Tao, Lizhong Li, Charles L Tschirhart, Evgeny Redekop, Kenji Watanabe, Takashi Taniguchi, et al. Realization of the Haldane Chern insulator in a moiré lattice. *Nature Physics*, 20(2):275–280, 2024.
- [44] Arthur Marguerite, John Birkbeck, Amit Aharon-Steinberg, Dorri Halbertal, Kousik Bagani, Ido Marcus, Yuri Myasoedov, Andre K Geim, David J Perello, and Eli Zeldov. Imaging work and dissipation in the quantum hall state in graphene. *Nature*, 575(7784):628–633, 2019.
- [45] T Jalabert, EFC Driessen, F Gustavo, JL Thomassin, F Levy-Bertrand, and C Chapelier. Thermalization and dynamics of high-energy quasiparticles in a superconducting nanowire. *Nature Physics*, 19(7):956–960, 2023.
- [46] Martin E Huber, Nicholas C Koshnick, Hendrik Bluhm, Leonard J Archuleta, Tommy Azua, Per G Björnsson, Brian W Gardner, Sean T Halloran, Erik A Lucero, and Kathryn A Moler. Gradiometric micro-SQUID susceptometer for scanning measurements of mesoscopic samples. *Review of Scientific Instruments*, 79(5):053704, 2008.

- [47] Beat Jeckelmann and Blaise Jeanneret. The quantum Hall effect as an electrical resistance standard. *Reports on Progress in physics*, 64(12):1603, 2001.
- [48] Al L Éfros and Boris I Shklovskii. Coulomb gap and low temperature conductivity of disordered systems. *Journal of Physics C: Solid State Physics*, 8(4):L49, 1975.
- [49] M Furlan. Electronic transport and the localization length in the quantum Hall effect. *Physical Review B*, 57(23):14818, 1998.
- [50] DJ Thouless. Field distribution in a quantum Hall device. *Journal of Physics C: Solid State Physics*, 18(33):6211, 1985.
- [51] JR Kirtley, Z Schlesinger, TN Theis, FP Milliken, SL Wright, and LF Palmateer. Voltage-controlled dissipation in the quantum Hall effect in a laterally constricted two-dimensional electron gas. *Physical Review B*, 34(8):5414, 1986.

Methods

Sample growth and sample fabrication

We used a VEECO 620 molecular beam epitaxy (MBE) system to grow heterostructures comprised of 3 quintuple layer (QL) $\text{Cr}_{0.15}(\text{Bi}, \text{Sb})_{1.85}\text{Te}_3$ - 5QL $(\text{Bi}, \text{Sb})_{1.85}\text{Te}_3$ - 3QL $\text{Cr}_{0.15}(\text{Bi}, \text{Sb})_{1.85}\text{Te}_3$ on SrTiO_3 (111) substrates (MTI Corporation). The Cr composition is nominal (based on past calibrations). The SrTiO_3 substrates were cleaned using deionized water at 90°C for 1.5 hours and thermally annealed at 985°C for 3 hours in a tube furnace with flowing oxygen gas. The substrate was out-gassed under vacuum at 630°C for 1 hour and then cooled down to 340°C for the heterostructure growth. When the temperature of substrate was stable at 340°C , high-purity Cr (5N), Bi (5N), Sb (6N), and Te (6N) were evaporated from Knudsen effusion cells to form the heterostructure. The desired beam equivalent pressure (BEP) fluxes of each element and the growth rate were precisely controlled by the cell temperatures. The BEP flux ratio of $\text{Te}/(\text{Bi} + \text{Sb})$ was kept higher than 10 to prevent Te deficiency. The BEP flux ratio of Sb/Bi was kept around 2 to tune the chemical potential of the heterostructure close to the charge neutrality point. The heterostructure growth rate was 0.25 QL/min, and the pressure of the MBE chamber was maintained at 2×10^{-10} mbar during the growth.

After the growth, the heterostructures were fabricated into a $200\ \mu\text{m} \times 75\ \mu\text{m}$ Hall bar and a two-terminal sample using photolithography. The shape of the samples was defined by Argon plasma etching. After etching, 10 nm Cr/60 nm Au were deposited outside the active area of the Hall bar to make electrical contact. The top gate was fabricated by depositing a 40 nm Al_2O_3 layer by atomic layer deposition across the entire sample and evaporating a 10 nm Ti/60 nm Au layer patterned by optical lithography.

Electronic transport characterization

Electrical connection to the samples were made via thermocoax lines in a cryogen-free dilution refrigerator with a base temperature of $\sim 15\ \text{mK}$ at the mixing chamber plate. Samples are mounted on a high thermal conductivity copper cold finger in the bore of a 6T-1T-1T vector magnet. We use the reference output of a Stanford Research Systems SR830 lock-in amplifier to excite one current contact of our Hall bar with a sinusoidal excitation at a frequency of 140.5 Hz while leaving the other current contact grounded. The longitudinal and Hall voltages are amplified by Stanford Research Systems SR540 preamplifiers before being demodulated by two lock-in amplifiers. The carrier density in the sample was tuned using the sample back gate formed by the SrTiO_3 substrate. During electrical transport characterization and current density imaging, the top gate was grounded.

Measurement of R_{th} with the 3ω method

To measure the thermal resistance characterizing energy relaxation from the electrons to the environment, we use the temperature-dependent resistance of the sample as a thermometer. We source a current $I = I_o \sin \omega t$

through the sample, generating heat in the sample at both DC and at 2ω . The input power P_{in} generates a temperature difference between the electrons at temperature T_e and the phonon bath at temperature T_p . At the low frequencies used in our experiments, this temperature difference appears in-phase with the the heat flow into the sample and R_{th} may be defined,

$$R_{th} = \frac{\Delta T}{P_{in}},$$

Where $\Delta T = T_e - T_p$, is the difference between the electron and phonon temperatures. The change in T_e in response to the input power causes the sample resistance to change. For small ΔT , $R_{xx}(T)$ may be expressed,

$$R_{xx}(T_e) = R_{xx}(T_p) + \frac{dR}{dT}\Delta T = R_{xx}(T_p) + \frac{dR}{dT}R_{th}(T_p)R_{xx}(T_p)I^2,$$

Where we have used $P_{in} = R_{xx}(T_p)I^2$. Next we introduce the time-dependence of the bias current, $I = I_o \sin \omega t$, and write the voltage drop over the sample using $V(t) = I(t)R(T)$,

$$V_{1\omega}(t) = I_o R(T_p) \left[1 + \frac{3}{4} \frac{dR}{dT} I_o^2 R_{th} \right] \sin \omega t$$

$$V_{3\omega}(t) = -I_o R(T_p) \left[\frac{1}{4} \frac{dR}{dT} I_o^2 R_{th} \right] \sin 3\omega t$$

where $V_{1\omega}(t)$ and $V_{3\omega}(t)$ are the first and third harmonic components of the voltage drop over the device. In a lock-in measurement, the the amplitude of the third-harmonic voltage may then be used to extract R_{th} ,

$$R_{th} = \frac{4V_{3\omega}}{I_o^3 R(T_p) \alpha},$$

where $\alpha = dR/dT$. We use $R_{xx}(T_p)$ measured with $I_o = 2$ nA, where bias-induced heating is negligible, to calculate dR/dT . We then extract the slope of $V_{3\omega}$ vs. I_o^3 in the low-bias ($I_o < 10$ nA) limit at a range of lattice temperatures T_p . Using $R_{xx}(T_p)$ and its derivative, we calculate R_{th} from the extracted slope of the $V_{3\omega}$ signal. At the lowest values of T_p , where both R_{xx} and dR/dT vanish, this analysis becomes unreliable. We therefore extract R_{th} only for $T_p > 60$ mK. R_{th} may also be extracted from the $V_{1\omega}$ signal after subtracting the Ohmic contribution, comparison between the two analysis methods is described in Supplementary Section: Consistency checks for 3ω technique.

Extraction of T_e from transport

To calculate the steady-state temperature difference $T_e - T_p$ between the electrons and the phonons, we start with the condition of energy balance, which dictates $P_{in} = P_{out}$ once the system reaches steady state [27, 28]. We use the resistance R_{xx} and RMS bias current I_b determined by lock-in measurements to estimate the input power $P_{in} = I_b^2 R_{xx}$. The power dissipated to the environment is related to R_{th} by $dP_{out} = (1/R_{th}) dT$. We integrate dP_{out} from T_p to T_e to obtain P_{out} and set $P_{out} = P_{in}$,

$$P_{in} = R_{xx} I_b^2 = \int_{T_p}^{T_e} \frac{dT}{R_{th}(T)}.$$

Evaluating the integral yields a simple relation between P_{in} , T_e and T_p ,

$$P_{in} = \frac{A\Sigma}{5} [T_e^5 - T_p^5], \quad (2)$$

Where we have used $R_{th} = (A\Sigma)^{-1}T^{-4}$, with $A\Sigma = 4.6 \times 10^6$ K⁵/W extracted from R_{th} measurements performed with the 3ω method to arrive at the analytical expression above. Here $A = 75 \mu\text{m} \times 300 \mu\text{m}$ is the area of the $\text{Cr}_{0.15}(\text{Bi}, \text{Sb})_{1.85}\text{Te}_3$ channel and $\Sigma \approx 10$ W/m²K⁵ is the intrinsic thermal relaxation strength of our $\text{Cr}_{0.15}(\text{Bi}, \text{Sb})_{1.85}\text{Te}_3$ heterostructure. In practice, $R_{xx}(I)$ is dependent on the RMS bias current I_b we use. We expect our estimate of P_{in} using a lock-in method to determine R_{xx} to be reasonably accurate

as long as the first-harmonic response of the sample dominates the time-dependent voltage drop over the sample for all I_b . We have verified that the first harmonic response of our sample is at least an order of magnitude larger than the second and third harmonic responses, indicating that this approximation is indeed valid for our sample. For samples where $R_{xx}(I)$ is monotonically increasing with I , our estimate of P_{in} will systematically over-estimate the true power dissipated the sample, due to the lock-in amplifier performing a weighted average of the sample resistance which is more heavily weighted towards values at higher currents, where the resistance is higher. Once the temperature dependence of R_{th} is known, the expression Eq.2 may be rearranged to solve for T_e for a given T_p and P_{in} ,

$$T_e = \left[\frac{5P_{in}}{A\Sigma} + T_p^5 \right]^{1/5}.$$

Scanning SQUID microscopy

Unless otherwise indicated, magnetic imaging was performed with a sample cooled below 50 mK in a cryogen free dilution refrigerator, described elsewhere [18]. The scanning SQUID sensor has the same gradiometric design as described in Ref. [46] with a 1.5 μm inner-diameter pickup loop. The SQUID is coupled to a SQUID-array amplifier mounted on the mixing chamber plate of the dilution refrigerator. We use a home-built piezoelectric scanner to scan the SQUID $\sim 1 \mu\text{m}$ above the sample surface. To measure the response of the sample to a bias current, we excite one contact of the sample with a sinusoidal excitation at a frequency of 140 Hz from the reference output of a Stanford Research Systems (SRS) SR830 lock-in amplifier. We ground the other current contact and use the four voltage probes to record the longitudinal and Hall potential drops over the sample using a pair of SRS SR540 preamplifiers. The SQUID signal and the output of the voltage preamplifiers are demodulated by SR830 lock-in amplifiers. We demodulate the SQUID signal at both the first and second harmonic of the excitation frequency in order to measure Φ_{1f} and Φ_{2f} respectively. In this work, the first harmonic signals, including Φ_{1f} , are the in-phase component of the demodulated signal. In a lock-in measurement, the second harmonic response in the sample due to heating effects appears 90° out-of-phase with the reference signal. We therefore present the quadrature component of the demodulated lock-in signal for the Φ_{2f} data reported here. Care was taken to measure at a sufficiently low frequency such that out-of-phase components (the quadrature signal for the Φ_{1f} data and the in-phase signal for the Φ_{2f} data) were minimized.

Current and magnetization reconstruction

Given that the sample thickness is more than an order of magnitude smaller than both the SQUID pickup loop radius and scan height, we treat the current density and the magnetization as two-dimensional in our analysis. The magnetic flux $\Phi(x, y)$ at lateral position x, y at height z above the sample detected by the SQUID is then given by the convolution of the SQUID point spread function, K_{PSF} , and the appropriate Biot-Savart kernel, K_{BS} ,

$$\Phi(x, y) = K_{\text{PSF}}(x, y) * K_{\text{BS}}(x, y) * g(x, y). \quad (3)$$

Where $*$ denotes a convolution defined by,

$$f(x, y) * h(x, y) = \int dx' dy' f(x', y') h(x' - x, y' - y). \quad (4)$$

The scalar function $g(x, y)$ may be interpreted as the magnetic dipole density, when reconstructing the sample magnetization. When flux is coupled into the SQUID by a transport current distribution, $g(x, y)$ may alternatively be identified as the current stream function, which is related to the two-dimensional current density by,

$$\vec{j}(x, y) = \nabla \times [g(x, y)\hat{z}]. \quad (5)$$

In two dimensions, K_{BS} is given by,

$$K_{\text{BS}} = \frac{\mu_o}{2\pi} \frac{2z^2 - x^2 - y^2}{(x^2 + y^2 + z^2)^{5/2}}. \quad (6)$$

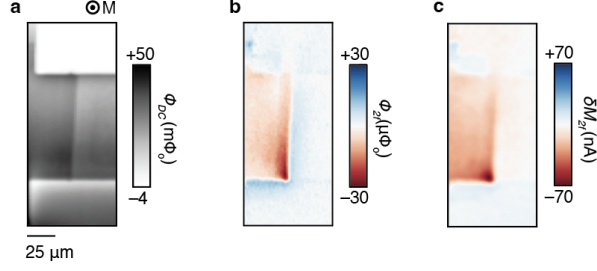


Figure ED1: **Hot spot location changes for reversed magnetization** **a**, DC flux Φ_{DC} , coupled into the SQUID pickup loop while imaging near the interface between the metal contact and semiconducting channel. The sample magnetization is reversed relative to the configuration in the main text (magnetized out-of-the plane). **b**, Second harmonic SQUID signal, Φ_{2f} recorded near the contact with the magnetization opposite to that of Fig. 1. The bias current I_b is 60 nA. **c**, Change in the sample magnetization δM_{2f} from bias-induced heating, reconstructed from **(b)**.

We extract K_{PSF} shown in from images of superconducting vortices acquired using a nominally identical SQUID. Reconstruction of $g(x, y)$ from a measured image $\Phi(x, y)$ which includes experimental noise is a deconvolution problem. Deconvolution problems require regularization to avoid the amplification of high spatial frequency noise in the final solution. Here we combine K_{PSF} and K_{BS} into a single linear operator M such that eq. 3 can be written as $\Phi = Mg$, where now g is a vector with length n equal to the number of pixels in an image and M is a $n \times n$ matrix. We chose a regularization operator Γ that penalizes solutions that include high-frequency noise, with a regularization strength σ . We seek the g^* that optimizes,

$$g^* = \min_g \left[\frac{1}{2} \|Mg - \phi\|^2 + \sigma^2 \|\Gamma g\|^2 \right]. \quad (7)$$

g^* can be found by solving the linear equation,

$$(M^T M + 2\sigma^2 \Gamma^T \Gamma)g = M^T \phi. \quad (8)$$

M^T and Γ^T are the pseudo-inverse of M and Γ , respectively. In practice, we do not directly calculate the elements of M , but instead calculate the convolution Mg using Fast Fourier transforms. We use the Wiener filter to approximate M^T and choose the discrete Laplace operator as our regularization operator Γ . For the one-dimensional line cut data, we utilize the same methods described above in one dimension. In this case, the SQUID point spread function and Biot-Savart kernel are integrated along one axis to form a 1D point spread function.

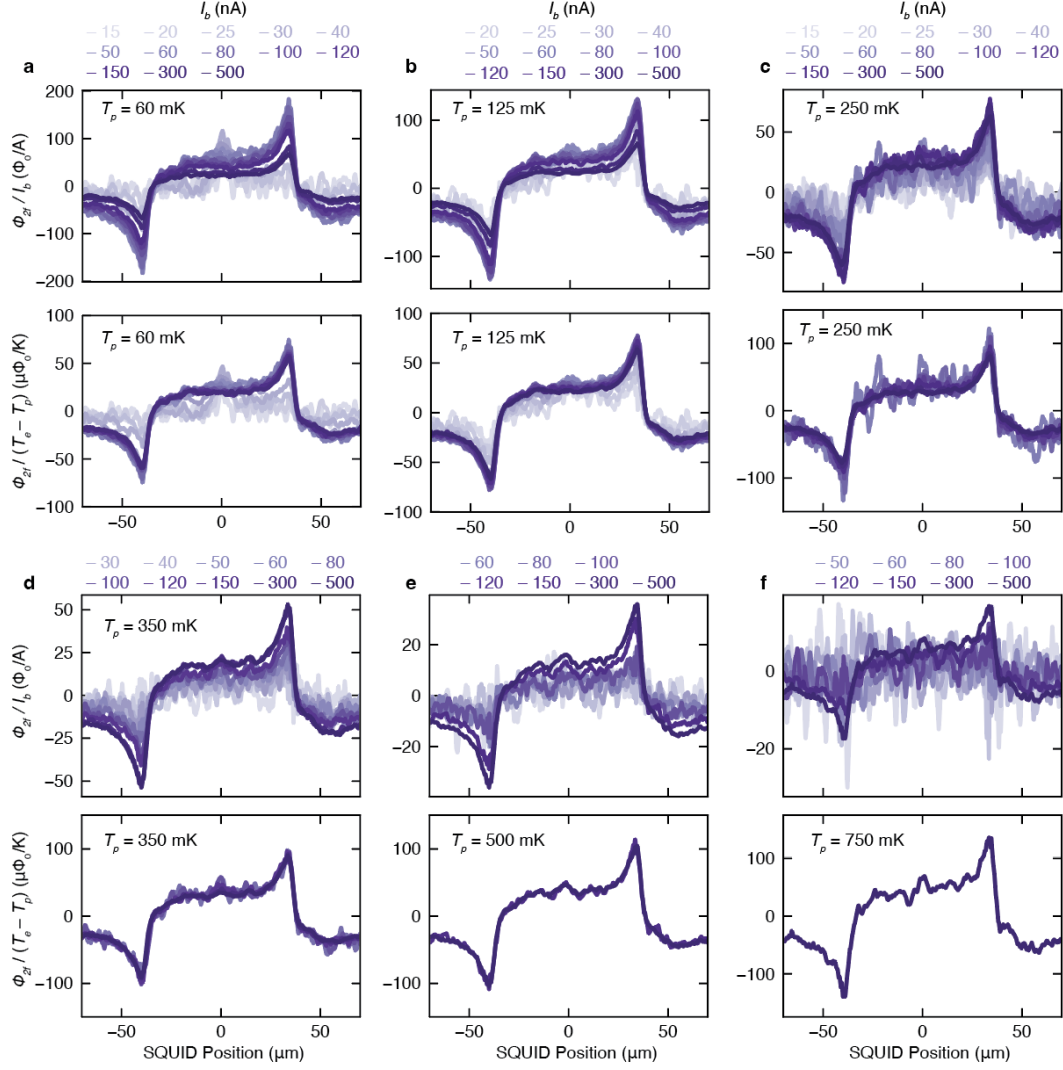


Figure ED2: **Magnetic signatures of heating at higher T_p** **a**, (top) Φ_{2f} signal acquired scanning over the width of the channel as in Fig. 4b, at a selection of source-drain bias currents I_b . Traces are normalized by I_b . $T_p = 60$ mK. (bottom) Φ_{2f} signal normalized by temperature difference $T_e - T_p$ predicted from the heating model described in the main text. Traces with $T_e - T_p < 25$ mK are omitted for clarity. **b**, same as **(a)**, with $T_p = 125$ mK. **c**, same as **(a)**, with $T_p = 250$ mK. **d**, same as **(a)**, with $T_p = 350$ mK. **e**, same as **(a)**, with $T_p = 500$ mK. **f**, same as **(a)**, with $T_p = 750$ mK.

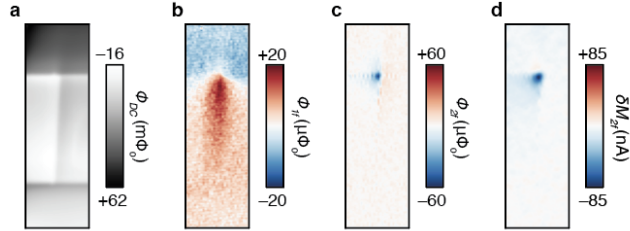


Figure ED3: **Imaging bias-induced heating at elevated T_p** **a**, DC flux, Φ_{DC} , coupled into the SQUID pickup loop while imaging the interface between the Au contact and the channel. The sample is magnetized into the plane. **b**, First harmonic SQUID signal Φ_{1f} co-recorded with the image in **(a)**. The bias current I_b is 150 nA. **c**, Second harmonic SQUID signal, Φ_{2f} co-recorded with the images **a,b**. At elevated T_p , Φ_{2f} is suppressed compared to the $T_p = 15$ mK case shown in Fig. 1d in the main text. **d**, Change in the sample magnetization δM_{2f} reconstructed from **(c)**. Data presented here was acquired with $T_p = 750$ mK. The amplitude and spatial extent of δM_{2f} is reduced compared to the $T_p < 50$ mK case shown in Fig. 1f in the main text.

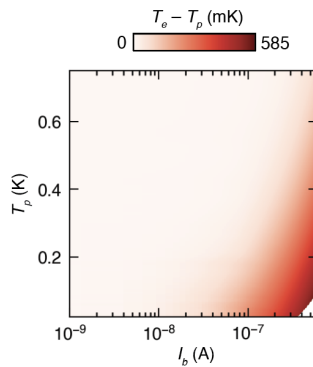


Figure ED4: **I_b and T_p dependence of heating effect** Amplitude of the heating effect $T_e - T_p$, calculated within the hot-electron model as a function of the bias current I_b and the lattice temperature T_p .

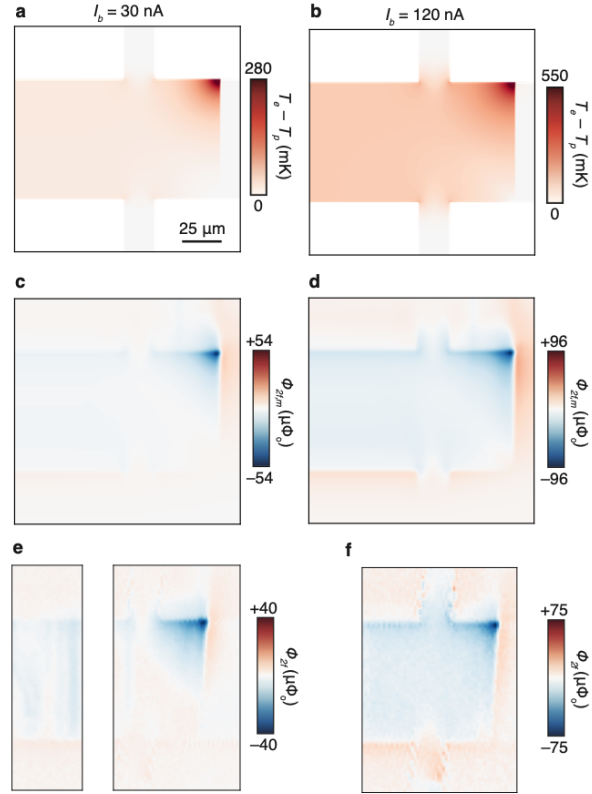


Figure ED5: **Comparison of the heating model at different I_b** **a**, Profile of the temperature difference between the electrons and phonons, calculated using the heating model for a bias current $I_b = 30$ nA. Model parameters are chosen to match the experimental conditions presented in Fig. 2c. **b**, Same as (a) for $I_b = 120$ nA. Model parameters are chosen to match the experimental conditions presented in Fig. 1e. Image of the model second harmonic SQUID signal $\Phi_{2f,m}$, calculated using the temperature distribution in (a) and assuming a magnetization temperature dependence of $\alpha = 300$ nA/K. **b**, Same as (c), calculated using the temperature profile in (b). **e**, Experimental Φ_{2f} measured for $I_b = 30$ nA. Data in (e) were used to reconstruct δM_{2f} in Fig. 2c. **f**, Same as (e), measured with $I_b = 120$ nA. Data in (f) reproduced from Fig. 1g.

Supplementary Information

Supplementary Section 1: Fitting different models for the conductivity

To compare the electronic transport behavior of our device to previous work on the breakdown of the QAHE, we fit the conductivity of our sample to several different models for hopping transport [11]. In Fig. S1 we show fits of the temperature dependence of σ_{xx} to three different models, with the devices tuned into the QAH regime with the back gate. In our device, the temperature dependence of σ_{xx} levels off at the lowest temperatures measured. To make a fair comparison between the three models, we perform each fit over the same temperature range. By adjusting the temperature interval over which the fit is performed, good agreement between the any of the models and the data can be obtained. In Fig. S1a, we show a fit to a model for thermally activated conduction with $\sigma_{xx} = \sigma_o e^{-T_o/T}$. In Fig. S1b, we show a fit to a model for variable range hopping, with $\sigma_{xx} = \sigma_o e^{-(T_1/T)^\alpha}$. Here, T_1 is the characteristic temperature scale of the hopping processes and $\alpha = 1/(d+1) = 1/3$ is determined by the number of spatial dimensions. In integer quantum Hall systems, the Coulomb interaction is predicted to suppress the density of states available for hopping conduction, leading to the modification of $\alpha = 1/2$ in the variable range hopping formula [47–49]. In Fig. S1c, we fit show a fit of our conductivity data using the variable range hopping formula with $\alpha = 1/2$ over the same temperature interval as the fit in Fig. S1a and S1b. Although we find the best agreement over the largest temperature window for the variable range hopping model including the effects of the Coulomb interaction, fits of similar quality with the other two models may be obtained by performing the fit over a slightly smaller temperature interval.

Supplementary Section 2: Resistor network model

To calculate the electrostatic potential and current distributions in our device, we follow the approach of Sample *et al.* [19] and model our device as a grid of nodes on which the electrostatic potential V is defined. The nodes on this grid are linked by a network for resistors with each node being connected to its nearest neighbors by two resistors. The first resistor encodes the effects of the longitudinal conductivity and supports a current proportional to the longitudinal potential drop between the nodes. The second resistor encodes the Hall effect, and it supports a current proportional to the transverse potential drop between the nodes. This approach allows us to model devices with an inhomogeneous conductivity tensor, which is important for modeling the interfaces between $\text{Cr}_{0.15}(\text{Bi},\text{Sb})_{1.85}\text{Te}_3$ and metallic contacts as well as regions inside the $\text{Cr}_{0.15}(\text{Bi},\text{Sb})_{1.85}\text{Te}_3$ channel which support a temperature gradient and therefore a spatially varying conductivity. In the special case of devices with a uniform conductivity tensor, our resistor network model produces potential distributions equivalent to those obtained with direct numerical solutions of the Laplace equation [15, 50], or the conformal mapping approach [51].

We represent the nodes in the network and the coupling between them as a sparse matrix encoding the set of linear equations generated by applying Kirchhoff's current and voltage laws to each node in the network. We calculate the electrostatic potential distribution inside our device using standard numerical methods to solve the system of equations.

Once the electrostatic potential distribution is determined, the current distribution is calculated using the conductivity tensor and Ohm's law:

$$j_x = \sigma_{xx}E_x + \sigma_{xy}E_y, \quad (9)$$

$$j_y = \sigma_{yx}E_x + \sigma_{yy}E_y, \quad (10)$$

where we have assumed $\sigma_{xx} = \sigma_{yy}$. To compare the calculated current distributions with our magnetic imaging data, we convolve the current distribution with the point spread function of our imaging technique. This procedure generates a model image, $\Phi_{1f,m}$ image, which can be directly compared to experimental Φ_{1f} images.

In Fig. S2, we compare the calculations of the resistor network model to magnetic imaging data as we tune the Hall angle using the back gate voltage. To compare the current distributions generated by the resistor network model to our magnetic imaging data, we convolve the model current distribution with the SQUID point spread function to generate a model magnetic flux image which may be directly compared to

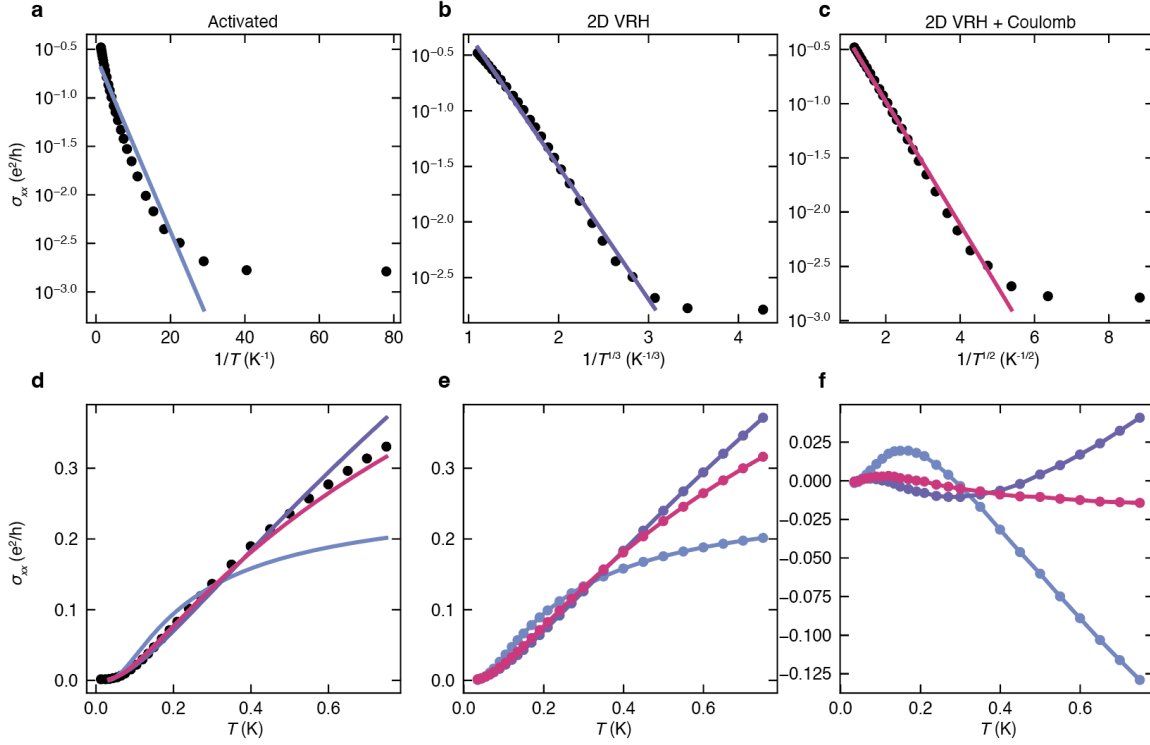


Fig. S1: **Fits to models for the low-temperature conductivity** **a**, Temperature dependent σ_{xx} (black) fit to an activated conductivity of the form $\sigma_{xx} = \sigma_o e^{-T_o/T}$ (blue). The fit is performed over data with $T > 30$ mK. The parameter $T_o = 90$ mK is extracted from the fit. **b**, Same as **(a)**, with the fit performed to a two-dimensional model for variable range hopping, $\sigma_{xx} = \sigma_o \exp[-(T_1/T)^{1/3}]$. The fit is performed over the same range of temperature as in **(a)**. The fit parameter $T_1 = 1.7$ K is extracted from the fit. **c**, Same as **(b)**, with a fit to 2D variable range hopping with the coulomb interaction, $\sigma_{xx} = \sigma_o \exp[-(T_1/T)^{1/2}]$. The fit parameter $T_1 = 0.32$ K is extracted from the fit. **d–e** Comparison between the three models presented in **a–c** and the data (black) on a linear scale. **f** Residuals for the three models.

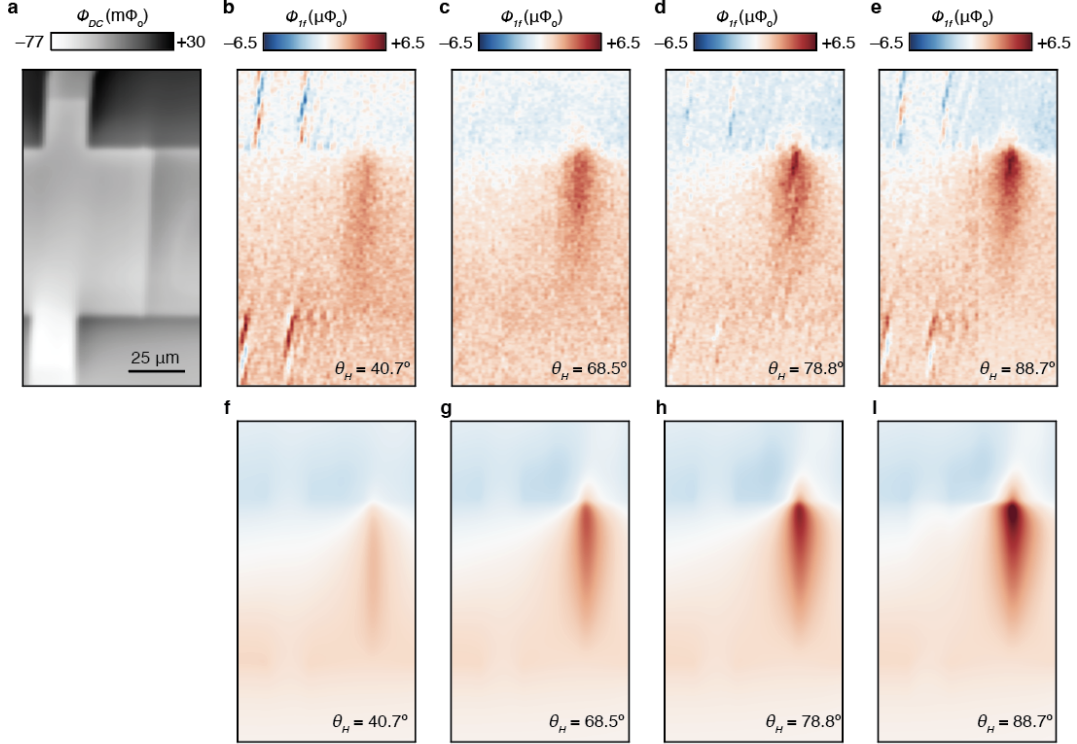


Fig. S2: V_{BG} dependence of the hot-spot current distribution **a**, DC flux Φ_{DC} coupled into the SQUID pickup loop while imaging the interface region between the semiconducting channel and metallic contact. **b**, First harmonic SQUID signal Φ_{1f} acquired with the sample tuned out of the QAH regime with $V_{BG} = 0$ V. The Hall angle determined via the resistivity is $\theta_H = 40.7$ deg. **c**, Same as (**b**) for $V_{BG} = 60$ V, $\theta_H = 68.5$ deg. **d**, Same as (**b**) for $V_{BG} = 77$ V, $\theta_H = 78.8$ deg. **e**, Same as (**b**) for $V_{BG} = 107$ V, $\theta_H = 88.7$ deg. **f**, Result of convolving the SQUID point-spread-function with the current distribution determined by the resistor network model with $\theta_H = 40.7$ deg in the channel. **g–i** Same as (**f**) with θ_H chosen to match the values measured for **c–e** respectively. Data presented in this figure were acquired at 15 mK.

the Φ_{1f} data. For the images in Fig. S2, we do not directly include the effects of heating, but instead set the Hall angle θ_H in the channel by hand to a value determined by the resistivity tensor.

In order to introduce the effects of heating to our model, we first convert the extrinsic R_{th} measured with the 3ω method to extract the intrinsic thermal relaxation strength, Σ in our $\text{Cr}_{0.15}(\text{Bi}, \text{Sb})_{1.85}\text{Te}_3$ sample,

$$R_{th}AT^4 = 0.1 \text{ K}^5 \text{ m}^2 / \text{W} = 1/\Sigma, \quad (11)$$

Where $A = 75 \mu\text{m} \times 300 \mu\text{m}$ is the area of the $\text{Cr}_{0.15}(\text{Bi}, \text{Sb})_{1.85}\text{Te}_3$ channel. We initialize our model with a uniform $T_e = T_p$. We use the resistivity of our device at T_p to assign the conductivity of the $\text{Cr}_{0.15}(\text{Bi}, \text{Sb})_{1.85}\text{Te}_3$ channel. Throughout the calculations, we take the metallic contacts to have a temperature-independent sheet conductivity of $\sigma_{xx} = 3 \text{ S}$ and $\sigma_{xy} = 0$. Next we solve for the electrostatic potential distribution and use Ohm's law as described above to determine the current distribution in the device. To determine the temperature distribution, we note that $p_{in} = p_{out}$ in steady state, where $p_{in} = j^2 \rho_{xx}$ is power per unit area applied to the sample for a given current density j . Similarly, $dp_{out} = \Sigma T^4 dT$ is the corresponding change in the power per unit area dissipated to the lattice, for an incremental temperature difference dT induced between the electrons and phonons. To calculate p_{out} , we integrate dp_{out} from T_p to T_e . Solving for T_e we obtain,

$$T_e = \left(\frac{5p_{in}}{\Sigma} + T_p^5 \right)^{1/5}, \quad (12)$$

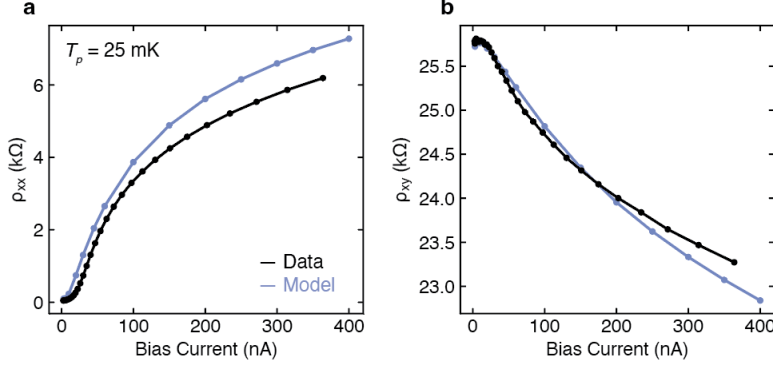


Fig. S3: **Consistency check for the resistor network model a**, Comparison of the resistivity of our device to the resistivity predicted by the resistor network model. The lattice temperature T_p , bias current I_b and thermal relaxation strength of $\text{Cr}_{0.15}(\text{Bi},\text{Sb})_{1.85}\text{Te}_3$ are supplied to the resistor network model. **a**, Longitudinal resistivity ρ_{xx} measured on our device (black) compared to the prediction of the model (blue) for the same T_p and I_b . **b**, Same as **a**, for the Hall resistivity ρ_{xy} .

With $j = \sqrt{j_x^2 + j_y^2}$. We calculate p_{in} using the current density determined by the model and the temperature dependence of ρ_{xx} measured on our device, allowing us to update the temperature distribution in the model.

From the updated temperature distribution, we re-calculate the conductivity of the sample using the temperature-dependent conductivity of our device. For the temperatures investigated in this work, the Hall conductivity of our device is nearly temperature independent, $\sigma_{xy}(T) \approx e^2/h$ and nearly all of the temperature dependence of ρ_{xx} and ρ_{xy} arises from the temperature dependence of σ_{xx} . For the purposes of our calculations it was sufficient to set $\sigma_{xy} = e^2/h$ and to update only σ_{xx} in our model. After updating the conductivity tensor, V may be recalculated using an updated sparse matrix which reflects the spatially inhomogeneous conductivity of the channel. The updated V may in turn be used to update p_{in} and the temperature distribution T_e . We have found that this approach converges rapidly to a steady-state temperature distribution. After ~ 10 updates, the size of updates to the electrostatic potential, δV , relative to the total electrostatic potential drop over the sample, V_b , is small for all nodes in the network with, $\delta V/V_b < 10^{-3}$. Similarly, after ~ 10 updates, further updates to the temperature distribution are much smaller than typical values of T_e , $\delta T_e/T_e < 10^{-3}$ for all nodes in the model. Introducing thermal relaxation processes in this way allows us to model the electrostatic potential, current and temperature distributions in our device by supplying only the lattice temperature T_p and the bias current I_b .

Our model is in principle sensitive to heating effects in the metallic contacts. We model the thermal relaxation strength in the contacts using $\Sigma = 2.4 \text{ Wm}^{-3}\text{K}^5$, a typical value measured at mK temperatures in metallic thin films [27, 28]. For 10 nm thick Au contacts, the thermal relaxation strength per unit area is roughly 2.4 times larger than the $\Sigma = 10 \text{ Wm}^{-2}\text{K}^5$ that we measured for $\text{Cr}_{0.15}(\text{Bi},\text{Sb})_{1.85}\text{Te}_3$. In practice, heating in the metallic contacts is negligible compared to the $\text{Cr}_{0.15}(\text{Bi},\text{Sb})_{1.85}\text{Te}_3$ channel due to the high σ_{xx} of the contact material compared to $\text{Cr}_{0.15}(\text{Bi},\text{Sb})_{1.85}\text{Te}_3$.

To check that the model reproduced the behavior of our device, we used the electrostatic potential distribution determined by our calculations to determine the resistivity of the network, which we directly compared to our electrical transport data. In Fig. S3, we compare the bias dependent resistivity of the resistor network model for $T_p = 25 \text{ mK}$.

Supplementary Section 3: Consistency checks for 3ω technique

In Fig. S4a-b we show the longitudinal and Hall resistance of our device as a function of I_b at a range of T_p between 65 mK and 750 mK. In Fig. S4c, we show the T_p dependence of R_{xx} (blue points) measured in the low-bias limit with $I_b = 2.5 \text{ nA}$. The R_{xx} is then interpolated (black) and used to determine dR/dT for the 3ω analysis.

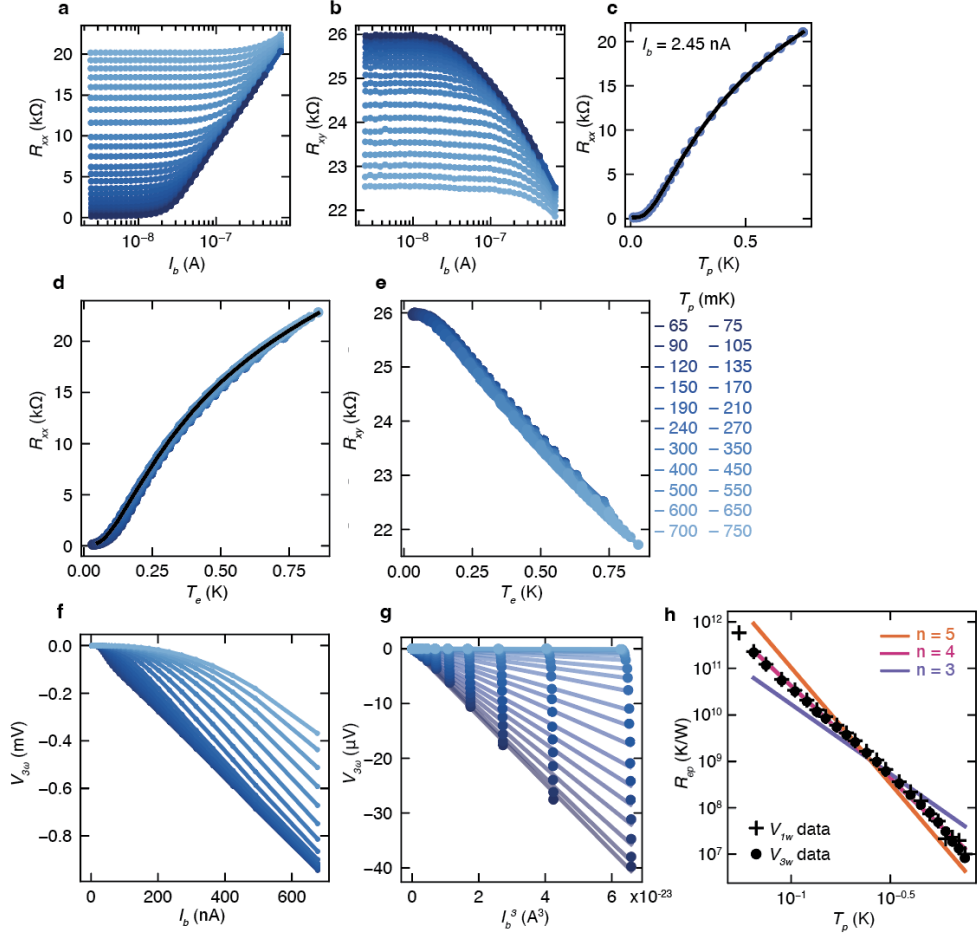


Fig. S4: **Measuring R_{th} with the 3ω method** **a**, Longitudinal resistance R_{xx} as a function of bias current, I_b and lattice temperature T_p . **b**, Hall resistance R_{xy} as a function of the bias current I_b and lattice temperature T_p . **c**, $R_{xx}(T_p)$ with $I_b = 2.45$ nA used to determine R_{xx} in the low-bias limit. An interpolated curve (black) is used to evaluate R_{xx} between the data (blue circles) when calculating R_{th} . **d**, R_{xx} from (a) with the temperature axis T_e calculated from the 3ω method. Reproduced from Fig. 3. **e**, Same as (d) for the R_{xy} data in (b). **f**, Third harmonic voltages, $V_{3\omega}$ measured as a function of I_b at different values of T_p . **g**, Same as (f), for $I_b < 40$ nA, plotted on a I_b^3 scale (circles). Linear fits to the data (lines) are used to extract R_{th} . **h**, Comparison between different analysis for extraction of R_{th} . R_{th} extracted from first harmonic $V_{1\omega}$ data (+), and R_{th} extracted from $V_{3\omega}$ (circles) are in quantitative agreement. Fits to the model $R_{th} \sim T^{-n}$ with n constrained to be 3, 4 and 5 are shown for comparison with the R_{th} data.

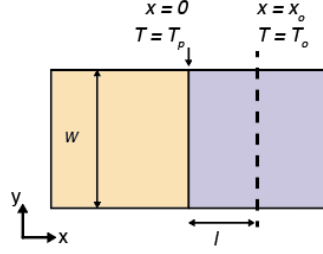


Fig. S5: **Estimating the electronic thermal conductance** Schematic of a simplified geometry used to estimate the electronic contribution to thermal relaxation in the channel. A metallic contact (yellow) of width w and $T = T_p$ makes contact to a semiconducting channel (purple) at $x = 0$. A distance l from the interface, at $x = x_o$, the electron temperature in the semiconducting channel is T_o .

In Fig. S4 d-e, same data as in Fig S4 a-b, with the resistance plotted against the effective electron temperature T_e calculated from the heating model described in the main text. Fig. S4d is reproduced from Fig. 3. Both R_{xx} and R_{xy} collapse onto a single curve indicating that bias-induced changes in the resistivity tensor of the sample may be understood in terms of changes in T_e .

In Fig. S4f, g we show the $V_{3\omega}$ signal measured as a function of I_b and T_p . Fig. SX f shows the $V_{3\omega}$ signal over a wide range of bias currents. Fig. S4 g shows the fit to the $V_{3\omega}$ signal near $I_b = 0$ which is used to extract R_{th} in the 3ω analysis.

As described in the main text and the methods, as the bias current heats the sample during our transport experiment, the temperature dependence of R_{xx} generates a correction to the first-harmonic voltage detected in the lock-in measurement,

$$V_{1\omega}(t) = I_o R(T_p) \left[1 + \frac{3}{4} \frac{dR}{dT} I_o^2 R_{th} \right] \sin \omega t,$$

As well as a third harmonic voltage which can also be detected using a lock-in amplifier,

$$V_{3\omega}(t) = -I_o R(T_p) \left[\frac{1}{4} \frac{dR}{dT} I_o^2 R_{th} \right] \sin 3\omega t.$$

In the main text, we use the third harmonic voltage, $V_{3\omega}$ to characterize the thermal relaxation from the electrons to their environment. R_{th} also generates a correction to the first harmonic voltage $V_{1\omega}$ as the bias current heats the sample. To verify the internal consistency of our analysis, we used the bias and T_p dependence of $V_{1\omega}$ data to extract R_{th} and compare the results to the $V_{3\omega}$ analysis in Fig. S4h. We find detailed and quantitative agreement in both the power-law dependence of R_{th} for both the $V_{3\omega}$ and $V_{1\omega}$ analysis. For comparison, we also present fits to the extracted R_{th} which are constrained to $n = 3$ (purple), $n = 4$ (magenta) and $n = 5$ (orange).

To estimate the statistical uncertainty in our best-fit values for n and Σ , we perform a linear fit to the temperature-dependent R_{th} on a log-log scale. We use the square root of the diagonal elements of the covariance matrix from this fit to estimate the uncertainty of n and Σ .

Supplementary Section 4: Estimate of the Electronic Thermal Conductance

To evaluate the importance of thermal conduction through the electronic subsystem to the contacts relative to the thermal relaxation processes described by R_{th} , we use the Wiedemann-Franz law estimate the thermal conductance through the electronic subsystem to a metallic contact. For simplicity, we consider the situation depicted schematically in Fig S5, with a $\text{Cr}_{0.15}(\text{Bi}, \text{Sb})_{1.85}\text{Te}_3$ channel of width w . A temperature gradient is imposed from the line at x_o where, $T = T_o$, to a metallic contact at temperature at T_p over a distance l . The electronic contribution to the thermal resistance $R_{th,e}$ to the contact is given by the Wiedemann-Franz law,

$$\frac{1}{R_{th,e}} = LT\sigma_{xx}(T)\frac{w}{l}, \quad (13)$$

Where $L = 2.44 \times 10^{-8} \text{ V}^2 \text{ K}^{-2}$ is the Lorenz number. To compare this thermal relaxation pathway to those provided by R_{th} , we compare $R_{th,e}$ to the R_{th} in area $A = l \times w$ between the contact and x_o ,

$$\frac{1}{R_{th}} = \Sigma A T^4 = \Sigma l w T^4 \quad (14)$$

Combining Eq. 13 and Eq. 14 to obtain the ratio between $R_{th,e}$ and R_{th} ,

$$\frac{R_{th,e}}{R_{th}} = \frac{\Sigma l^2 T^3}{L \sigma_{xx}}. \quad (15)$$

The relation Eq. 15 indicates that there is a length l_o from the contact beyond which the thermal resistance through the electrons $R_{th,e}$ becomes larger than R_{th} . Setting $R_{th,e} = R_{th}$ and substituting typical values for our experiment, $\sigma_{xx} \approx 10^{-2} \times e^2/h$, $\Sigma \approx 10 \text{ W/m}^2 \text{ K}^5$, $T_p = 50 \text{ mK}$, we find $l_o \approx 2.6 \mu\text{m}$. We expect this estimate for l_o to be appropriate at low temperatures, with small temperature gradients within the sample. In our experiments this limit is realized in the low-bias, low temperature limit.

Near the hot-spot, T_e exhibits large gradients which in turn generate large variations in σ_{xx} and R_{th} . In this case, we estimate $R_{th,e}$ and R_{th} taking into account the spatial variations in T . We continue to approximate the temperature gradient from x_o to the contact as a linear temperature drop. We choose $T_p = 50 \text{ mK}$ and $\delta T = T_o - T_p = 300 \text{ mK}$. For simplicity, we seek an upper bound on l_o by approximating $\sigma_{xx}(T) = \sigma_{xx}(T_o) \approx 10^{-1} \times e^2/h$ throughout the region, knowing that this approximation will over-estimate the true σ_{xx} near the contact, and therefore over-estimate the contribution of thermal conduction to the contact. For the electronic part of the thermal conductance we find,

$$R_{th,e} = \frac{1}{w \sigma_{xx} L} \int_0^l dx \frac{1}{\delta T \cdot (x/l) + T_p} \quad (16)$$

$$= \frac{l}{w \sigma_{xx} L (\delta T)} \ln \frac{T_o}{T_p} \quad (17)$$

And for the energy relaxation processes described by R_{th} we find,

$$\frac{1}{R_{th}} = \Sigma w \int_0^l dx [\delta T \cdot (x/l) + T_p]^4 \quad (18)$$

$$= \frac{\Sigma w l}{5(\delta T)} [T_o^5 - T_p^5]. \quad (19)$$

Combining Eqs. 17, 19 by setting $R_{th,e} = R_{th}$ in order to find an expression for l_o we obtain,

$$l_o^2 = \frac{5(\delta T)^2 L \sigma_{xx}}{\Sigma \cdot [T_o^5 - T_p^5] \ln(T_o/T_p)}. \quad (20)$$

Substituting the values above for large temperature gradients near the hot spot we estimate $l_o \approx 1.3 \mu\text{m}$. We therefore expect that in the case of both small temperature gradients appropriate for low I_b as well as large temperature gradients generated near the hot spot that conductive cooling to the contacts becomes an inefficient mode of energy relaxation beyond a few micrometers from the contact channel interface.